RSC Advances

PAPER

View Article Online
View Journal | View Issue

Cite this: *RSC Adv.*, 2023, **13**, 2811

Fabrication and catalytic properties of nanorod-shaped (Pt–Pd)/CeO_2 composites†

Haiyang Wang,‡[a] Wenyuan Duan,‡[a] Ruiyin Zhang,[a] Hao Ma,[a] Cheng Ma,[a] Miaomiao Liang,[b] Yuzhen Zhao[a] and Zongcheng Miao *[ac]

Received 21st November 2022
Accepted 19th December 2022

DOI: 10.1039/d2ra07395a

rsc.li/rsc-advances

Nanorod-supported (Pt–Pd)/CeO_2 catalysts were synthesized by a simple method of dealloying $Al_{91.7}Ce_8Pt_XPd_{0.3-X}$ (X = 0, 0.075, 0.1, 0.15, 0.2, 0.3) alloy ribbons. SEM and TEM characterization implied that after calcination treatment, the achieved resultants exhibited interspersed nanorod structures with a rich distribution of nanopores. Catalytic tests showed that the ($Pt_{0.1}$–$Pd_{0.2}$)/CeO_2 catalyst calcined at 300 °C exhibited the highest catalyst activity for CO oxidation when compared with other catalysts prepared at different noble metal ratios or calcined at other temperatures, whose complete reaction temperature was as low as 100 °C. The outstanding catalytic performance is ascribed to the stable framework structure, rich gas pathways and collaborative effect between the noble Pt and Pd bimetals.

1. Introduction

Because of the flammability and easy-explosion feature of CO, which is generated in daily life and industrial production, it is important to eliminate CO.[1] Even though the oxidation of CO to CO_2 is a good method to eliminate CO pollution, it always requires large energy consumption and strict conditions during the process. Catalytic oxidation of CO is an efficient method to get rid of CO pollution at low/room temperatures.[2–4] As the earliest proposed type of catalysts, noble metals such as Pd, Pt, Rh, and Au exhibit high activity for CO oxidation.[5–7] Pt group metal-based catalysts play an important role in the catalytic field because of their strong activity and wide applications, but the high price and low efficiency of a single atom of Pt hinder its further development.[8] Partial introduction of Pd, a cheaper noble metal into Pt can not only reduce the cost but can also enhance catalytic efficiency and avoid CO poisoning.[9,10] Suzanne Giorgio *et al.* achieved partial institution of Pt to Pd and obtained core–shell structured Pt–Pd nanotubes.[11] The Garcia's team synthesized bimetallic clusters by doping Pd into Au_{25} and demonstrated the strongly enhanced CO conversion of bimetallic catalysts.[12]

Ceria (CeO_2), a rare metal oxide with abundant reserves on the earth, is known to be a good supporting oxide for catalysis due to its outstanding store/release oxygen ability through a reversible and fast Ce^{4+}/Ce^{3+} reaction.[13–15] Moreover, the low energy for oxygen vacancy formation and oxygen diffusion as well as superior thermal stability makes CeO_2 an ideal material for gas catalytic usage. CeO_2-noble metal-based catalysts with rich morphologies and facets such as nanorods,[16] nanocubes,[17] particles,[18] and octahedra,[19] have been widely reported. The Neyman's group[20] synthesized Pt/CeO_2 catalyst with different Pt loading by a co-precipitation method and observed the CO oxidation activity at low temperatures. Xu and his collaborators[21] loaded Au on ZIF-8 successfully through the solid grinding method, and the obtained Au@ZIF-8 catalyst showed good activity. However, the preparation conditions for these catalysts usually need high economic costs with low yield, and their practical and industrial production is still a challenge.

Recently, the dealloying method has generated wide attraction for the preparation of nanomaterials because of its simple and effective fabrication features.[22,23] The morphology and size of materials can be controlled by changing corrosion or post-treatment conditions or by adjusting the composition and content of alloys. The CeO_2-noble metal-based catalysts, such as Rh/CeO_2,[24] Au/CeO_2,[25] and CeO_2-transition metal (oxide)-based catalysts such as baize-like NiO/CeO_2,[26] Cu/CeO_2,[27] have been successfully fabricated by a dealloying method and displayed outstanding catalytic activity for CO oxidation because of the large surface area and high porosity of the porous structured materials. However, the influence and mechanism of bimetal loading on CeO_2 need further investigation.

Inspired by the above considerations, herein, the nanorod-supported (Pt–Pd)/CeO_2 catalysts with varied Pt/Pd ratios were prepared by dealloying Al–Ce–Pt–Pd alloy ribbons followed by

[a]*Xi'an Key Laboratory of Advanced Photo-electronics Materials and Energy Conversion Device, Key Laboratory of Organic Polymer Photoelectric Materials, School of Electronic Information, Xijing University, Xi'an, 710123, P. R. China*

[b]*School of Materials Science and Engineering, Xi'an Polytechnic University, Xi'an, Shaanxi, 710048, P. R. China*

[c]*School of Artificial Intelligence, Optics and Electronics (iOPEN), Northwestern Polytechnical University, Xi'an, Shaanxi, 710072, P. R. China. E-mail: miaozongcheng@nwpu.edu.cn*

† Electronic supplementary information (ESI) available. See DOI: https://doi.org/10.1039/d2ra07395a

‡ These authors contributed equally to this work.

corrosion and calcination treatment for catalytic CO oxidation. Results show that the obtained samples exhibited stable framework structure and large amounts of pathways for gas entry/exit due to the interspersed nanorods and the joint effect of Pt/Pd as well as the formation of rich nanopores among nanorods. The $(Pt_{0.1}–Pd_{0.2})/CeO_2$ catalyst exhibited the best catalytic performance with 50% and 99% conversion at temperatures (T_{50}, T_{99}) as low as 75 °C and 100 °C, respectively.

2. Experimental section

2.1 Material preparation

The precursor alloy ingots of $Al_{92}Ce_8$, $Al_{91.7}Ce_8Pt_X–Pd_{0.3-X}$ (X = 0, 0.075, 0.1, 0.15, 0.2, 0.3) were fabricated from pure metal Al, Ce, Pt, Pd by arc-melting under high-purity Ar atmosphere. The obtained alloy ingots were then remelted in a quartz tube and blown onto a copper cooling roll to achieve an alloy ribbon with a width of 4–6 mm and a thickness of 40–70 μm. Next, the quenched ribbons were immersed into 20 wt% NaOH aqueous solution at room temperature for 2 hours until no bubbles generated and then further immersed at 353 K for 10 hours. Ultimately, the de-alloyed ribbons were dried and calcined at 473–773 K for 2 h in a pure O_2 environment. The samples derived from Al–Ce–Pt–Pd precursors were denoted as $(Pt_X–Pd_{0.3-X})/CeO_2$ (X = 0.075, 0.1, 0.15, 0.2). The subscript number of Pt and Pd in $(Pt_X–Pd_{0.3-X})/CeO_2$ refers to their respective atomic proportion in the $Al_{91.7}Ce_8Pt_XPd_{0.3-X}$ precursor.

2.2 Characterization

The phase composition was investigated by X-ray diffractometry (XRD, Bruker D8 Advance). The surface morphologies and microstructures of the fabricated catalysts were characterized by field emission scanning electron microscopy (FESEM, JEOL, JSM-7000F) and high-resolution transmission electron microscopy (HRTEM, JEOL, JEM-2100). EDS analysis and mapping were performed by scanning transmission electron microscopy (STEM, FEI-200) equipped with an Oxford Instrument's EDS spectrometer. The element composition and valence state were measured using an X-ray photoelectron spectrophotometer (XPS, ESCALAB Xi+). Nitrogen sorption isotherms and specific surface area were measured on a Micromeritics ASAP 2020 instrument at 77 K, and the pore size distributions were obtained from the desorption branch of the isotherm using the Barrett–Joyner–Halenda algorithm. Raman spectra were collected using an HR 800 fully automatic laser Raman spectrometer with a laser wavelength of 633 nm. Hydrogen temperature-programmed reduction (H_2-TPR) measurements were performed on an Auto ChemTM II 2920 chemisorption analyzer.

2.3 Catalytic evaluations

The catalytic performance of the fabricated catalysts was studied using a tube furnace with a fixed bed flow reactor under atmospheric pressure. A 100 mg tested sample was placed into the reactor and fixed with quartz wool. The feeding gas with a mixture of 1% CO, 10% O_2, and 89% N_2 (volume fraction) was injected into the test system at a flow rate of 100 mL min^{-1} and space velocity of 60 000 h^{-1}. The intake and outlet gases were analysed using an Anglit 7890B gas chromatograph equipped with a hydrogen flame detector (FID). The CO conversion can be calculated by eqn (1)

$$\text{CO conversion} = \frac{C_{in} - C_{out}}{C_{in}} \times 100\% \quad (1)$$

in which C_{in} and C_{out} represent the concentration of CO entering and exhausting the reactor, respectively.

3. Results and discussion

In this work, a facile combined dealloying and calcination method is proposed to fabricate a nanorod-supported bimetal/CeO_2 framework structure (Fig. S1†). The XRD patterns of the melt-spun ribbon precursor and de-alloyed $Al_{91.7}Ce_8Pt_{0.1}Pd_{0.2}$ ribbons are shown in Fig. S2,† while the de-alloyed ribbons with varied Pt/Pd content after calcination treatment are displayed in Fig. 1. As observed in Fig. S2,† the melt-spun ribbons consist of α-Al, $Al_{92}Ce_8$, and Al_4Ce phases; after the de-alloying treatment, the peaks representing α-Al, $Al_{92}Ce_8$ and Al_4Ce disappeared, while the new diffraction peaks corresponding to CeO_2 were detected, which may be due to the fact that the precursor ribbons decomposed during the de-alloying procedure. The XRD patterns of the four de-alloyed Al–Ce–Pt–Pd ribbons after calcination treatment are presented in Fig. 1; the diffraction peaks located at 28.64°, 33.06°, 47.56° 56.22° correspond to (111), (200), (220), (311) planes, respectively, of cubic CeO_2 (PDF# 89-8436).[28,29] No diffraction peaks corresponding to Al, Pt, and Pd were detected in the $(Pt_X–Pd_{0.3-X})/CeO_2$ samples (Fig. 1), demonstrating that Al has been completely removed from the material system. What is more, Pt and Pd were also not detected, which could be due to the low content and high dispersity of the two noble elements in the material system as well as the poor crystallinity of the samples.

The surface microstructures of the de-alloyed Al–Ce–Pt–Pd with varied Pt/Pd content calcined at 573 K were characterized by SEM (Fig. 2). The samples are composed of nanorods, which intersperse and stack each other to form a nanorod-supported

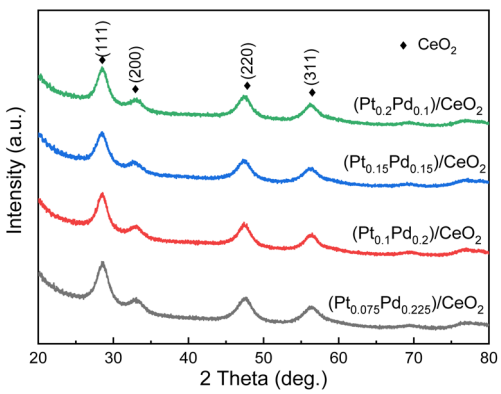

Fig. 1 XRD patterns of $(Pt_X–Pd_{0.3-X})/CeO_2$ (X = 0.075, 0.1, 0.15, 0.2) calcined at 573 K.

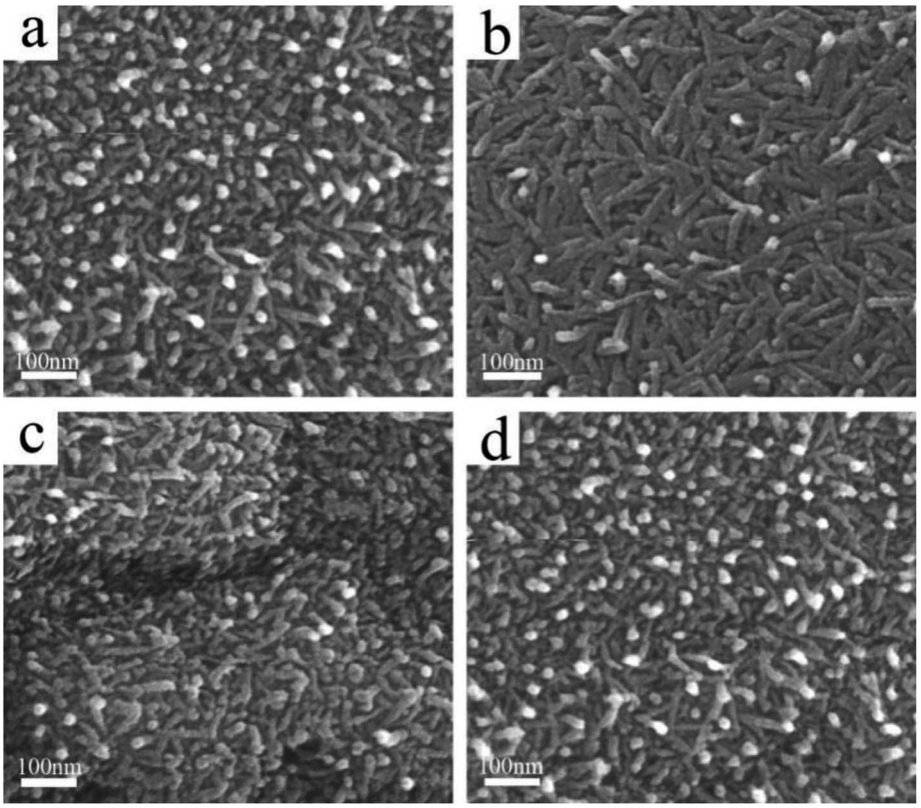

Fig. 2 The SEM images of $(Pt_X–Pd_{0.3-X})/CeO_2$ X = (a) 0.075, (b) 0.1, (c) 0.15, (d) 0.2.

framework structure with rich nanopores distributed among them. The diameter of nanorods is 5–10 nm. As the total content of Pt and Pd in Al–Ce–Pt–Pd alloy keeps 0.3 at%, and when the Pt content is increased to 0.075 at% (Fig. 2a), 0.1 at% (Fig. 2b), 0.15 at% (Fig. 2c) and 2 at% (Fig. 2d), respectively, the surface microstructure of the sample stayed similar and did not change significantly. However, the interspersed nanorods help stabilize the framework structure of samples; the existence of rich nanopores can provide more pathways for the gas to enter/exit, thus enhancing the catalytic oxidation rate.[24] The SEM images of $(Pt_{0.1}–Pd_{0.2})/CeO_2$ calcined at different temperatures are shown in Fig. S3.† As observed, even though the nanorods of $(Pt_{0.1}–Pd_{0.2})/CeO_2$ are coarsened after calcining at 300 °C, and 500 °C, when compared with samples without the calcination treatment, their overall morphology remained unchanged, implying outstanding thermal stability.

TEM studies were conducted to obtain a more detailed microstructure information of $(Pt_X–Pd_{0.3-X})/CeO_2$. As observed from the TEM images of $(Pt_{0.075}–Pd_{0.225})/CeO_2$ (Fig. 3a), $(Pt_{0.1}–Pd_{0.2})/CeO_2$ (Fig. 3c), $(Pt_{0.15}–Pd_{0.15})/CeO_2$ (Fig. 3e), $(Pt_{0.2}–Pd_{0.1})/CeO_2$ (Fig. 3g), the black nanoparticles with an average diameter of 3–5 nm are homogeneously loaded onto the surface of nanorod; the nanorod with an average diameter of 10 nm pile up on each other to form an interconnected structure, which is in line with SEM results. In the HRTEM images shown in Fig. 3b, d, f and h, the interplanar space of 0.32 nm corresponds to the (111) plane of the cubic structure of CeO_2 nanorods; the lattice fringe widths of 0.229 nm and 0.264 nm for the black particles semi-inlaid onto nanorod corresponded to the (111) and (101) planes of Pt and PdO, respectively, demonstrating that Pt and PdO were successfully loaded onto the CeO_2 nanorod surface. Noteworthy, the introduced Pt and PdO were close to each other, which helps the synergistic effect between them and promotes the respective adsorption and oxidation of CO during the catalytic process, thus contributing to the enhancement of the catalytic performance of (Pt–Pd)/CeO_2 catalysts.

STEM mapping characterization was utilized to analyze the distribution of elements on the surface of CeO_2 nanorods in $(Pt_{0.1}–Pd_{0.2})/CeO_2$ catalyst and the results are shown in Fig. 4. As clearly observed from Fig. 4a, Pt, and PdO are *in situ* loaded on the surface of CeO_2 nanorods in the form of nanoparticles (indicated by white arrows). Fig. 4b–d further demonstrates that the sample consists of Ce, Pt, and Pd elements, and they are homogeneously distributed among nanorods.

The N_2 adsorption–desorption studies were conducted to determine the surface area, pore size, and distribution in the samples. As shown from the nitrogen adsorption–desorption isotherms of four (Pt–Pd)/CeO_2 catalysts shown in Fig. 5a, all of them exhibit type-IV isotherm with a type-H3 hysteresis loop at a relative pressure range of 0.65–1.0 P/P_0, implying the existence of the mesoporous structure.[30] The BET surface areas of $(Pt_{0.075}–Pd_{0.225})/CeO_2$, $(Pt_{0.1}–Pd_{0.2})/CeO_2$, $(Pt_{0.15}–Pd_{0.15})/CeO_2$, $(Pt_{0.2}–Pd_{0.1})/CeO_2$ are 122.50, 120.19, 136.43, 132.54 $m^2\ g^{-1}$, respectively. What is more, the BHJ pore-size distribution curves in Fig. 5b present a uniform pore-size distribution located at 10–13 nm, further illustrating the mesoporous structure feature of

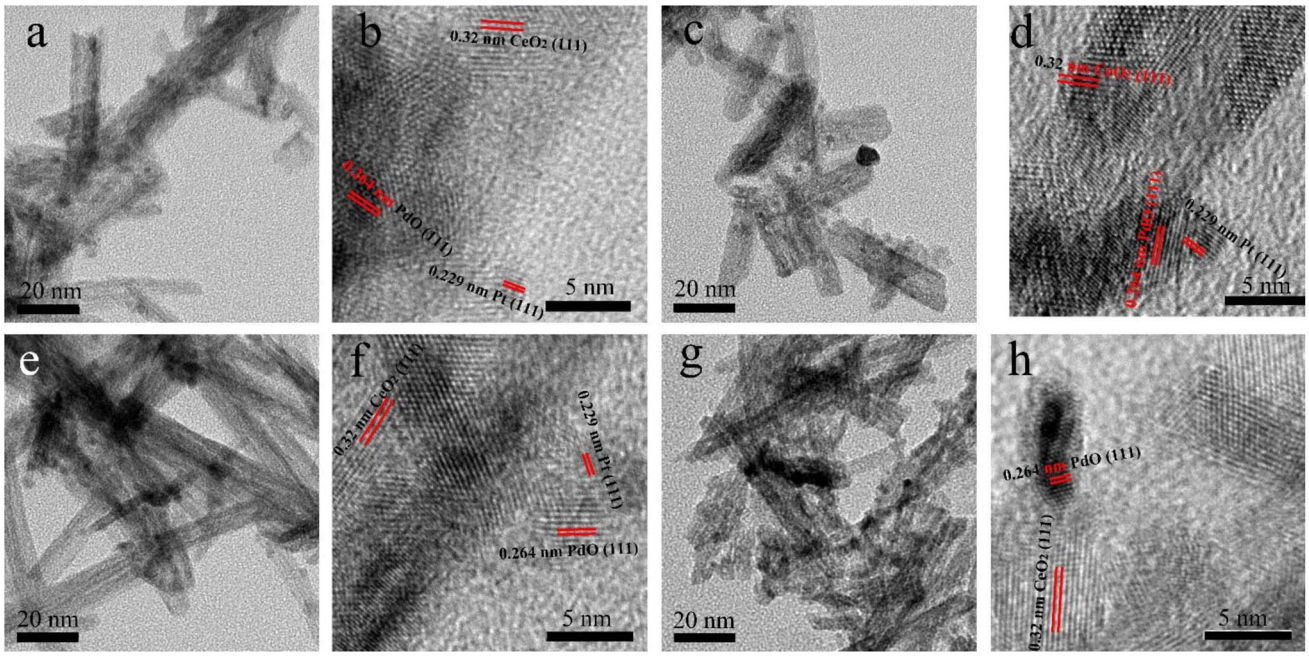

Fig. 3 The TEM and HRTEM images of (a and b) $(Pt_{0.075}–Pd_{0.225})/CeO_2$, (c and d) $(Pt_{0.1}–Pd_{0.2})/CeO_2$, (e and f) $(Pt_{0.15}–Pd_{0.15})/CeO_2$, (g and h) $(Pt_{0.2}–Pd_{0.1})/CeO_2$.

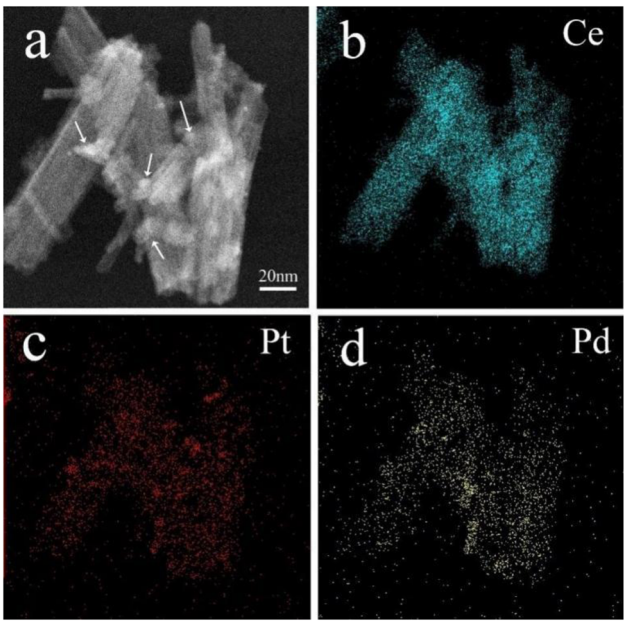

Fig. 4 (a) The STEM image of $(Pt_{0.1}–Pd_{0.2})/CeO_2$ and element mapping of (b) Ce, (c) Pt, (d) Pd.

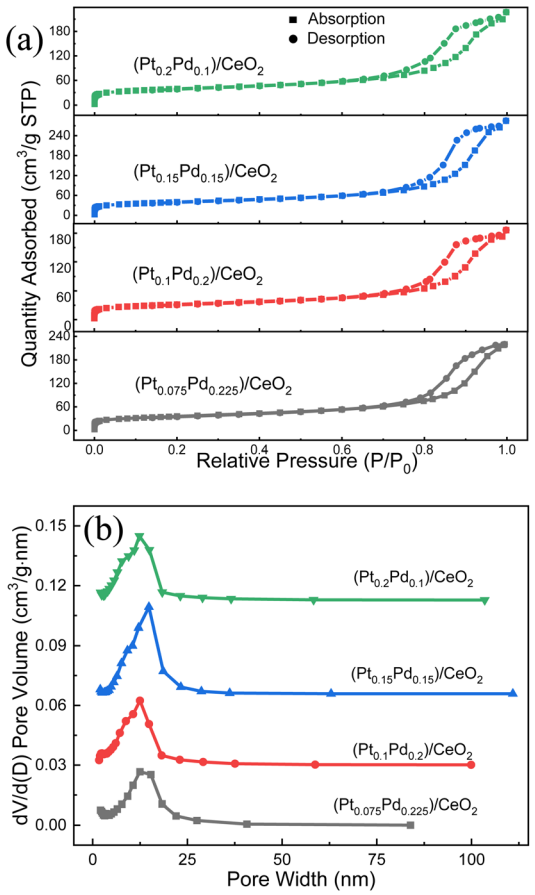

Fig. 5 (a) Nitrogen adsorption–desorption isotherms and (b) the BHJ pore size distribution of the de-alloyed (Pt–Pd)/CeO_2 nanorods.

the four samples.[31] The pore volumes for $(Pt_{0.075}–Pd_{0.225})/CeO_2$, $(Pt_{0.1}–Pd_{0.2})/CeO_2$, $(Pt_{0.15}–Pd_{0.15})/CeO_2$, $(Pt_{0.2}–Pd_{0.1})/CeO_2$ are 0.33, 0.33, 0.44, 0.34 $cm^3\ g^{-1}$. Obviously, all of the de-alloyed samples after the calcination treatment displayed higher specific surface area and lower pore diameter when compared with that of the pure CeO_2 nanorod framework reported in the previous work.[32] In addition, although the added proportion of

Pt and Pd varies as the total content stays unchanged, the partial replacement of Pt with Pd did not affect the physical structure parameters of the material significantly, so the specific surface area and porosity of the four samples are quite similar.

The chemical valence of the surface elements was confirmed using XPS and the typically fitted Ce 3d, Pt 4f, Pd 3d, O 1s XPS spectra of the $(Pt_{0.1}–Pd_{0.2})/CeO_2$ catalyst as obtained by the Gaussian fitting method, and presented in Fig. 6a–d, respectively. In Fig. 6a, the Ce 3d spectrum is fitted with six spin–orbit split doublets and two shake-up satellites. The binding energies at 881.9 eV, 888.2 eV, and 897.7 eV for Ce $3d_{5/2}$ and 900.4 eV, 907.3 eV, 916.2 eV for Ce $3d_{3/2}$ are characteristic of Ce^{4+}, and the peaks located at 884.5 eV, 903.3 eV are assigned to Ce^{3+}.[30,33] Since the concentration of Ce^{3+} can be reflected from the integrated areas of peaks, the surface Ce^{3+} concentration of total Ce on the $(Pt_{0.1}–Pd_{0.2})/CeO_2$ nanorod framework is 18.26% (Fig. 6a). In Fig. 6b, the two peaks at 70.9 eV and 74.2 eV are assigned to Pt^0,[34] while the binding energies at 72.1 eV for Pt $4f_{7/2}$ and 76.1 eV for Pt $4f_{5/2}$ correspond to Pt^{2+}.[35] Similarly, the 63.3% percentage of Pt^0 can be achieved by calculating the fitting areas of $Pt^0/(Pt^0 + Pt^{2+})$. In the Pd 3d spectrum shown in Fig. 6c, both metallic Pd and ionic Pd^{2+} can be clearly detected in $(Pt_{0.1}–Pd_{0.2})/CeO_2$ catalyst. The peaks at 336.2 eV and 341.2 eV correspond to Pd $3d_{5/2}$ of Pd^0; the binding energies at 337.2 eV for Pd $3d_{5/2}$ and 342.5 eV for Pd $3d_{5/2}$ belong to Pd^{2+}.[36] The Pd^{2+} concentration of total Pd is 71% and the ratio between Pd^0 and Pd^{2+} is around 3 : 7. For the O 1s spectrum in Fig. 6d, the peaks at 529.2 eV, 531.2 eV correspond to lattice oxygen (O_{lat}), surface adsorbed oxygen (O_{sur}), respectively.[37] The calculation results show that the ratio of O_{sur} can reach as high as 31%. Since O_{sur} with better activity can stabilize the sample structure and promote the catalytic oxidation rate, the high ratio of O_{sur} in $(Pt_{0.1}–Pd_{0.2})/CeO_2$ is beneficial for enhancing the catalytic property of $(Pt–Pd)/CeO_2$.

Raman studies were conducted to further illustrate the molecular structure of the samples. Four kinds of $(Pt–Pd)/CeO_2$ catalysts with varied Pt/Pd ratios, an apparent peak located at 456 cm^{-1} can be observed (Fig. 7a), which is attributed to the F_{2g} vibrational mode of CeO_2 originating from the breathing mode of oxygen anions around Ce cations.[38,39] Compared with the Raman result of pure CeO_2 shown in Fig. S4,† the peak intensity of $(Pt–Pd)/CeO_2$ catalysts is greatly decreased, and the diffraction location is shifted from 459 cm^{-1} to 456 cm^{-1}, which is due to the generation of more grain boundaries brought from grain refinement after the addition of Pt and Pd nanoparticles into the material system. H_2-TPR measurements were also adopted to investigate the reducibility of samples, as shown in Fig. 7b. For $(Pt_{0.075}–Pd_{0.225})/CeO_2$, $(Pt_{0.1}–Pd_{0.2})/CeO_2$, $(Pt_{0.15}–Pd_{0.15})/CeO_2$ and $(Pt_{0.2}–Pd_{0.1})/CeO_2$ catalysts, the H_2 consumption peaks were located around 110–120 °C and are assigned to Pt and Pd nanoparticles; the strong peak at around 470 °C is related to active oxygen species of CeO_2, whereas the reduction peaks at 700–800 °C are bonded to lattice oxygen of CeO_2 that is not closely related to catalytic capacity.[29,40] By contrast, the integrated peak area of active oxygen for $(Pt_{0.1}–Pd_{0.2})/CeO_2$ and

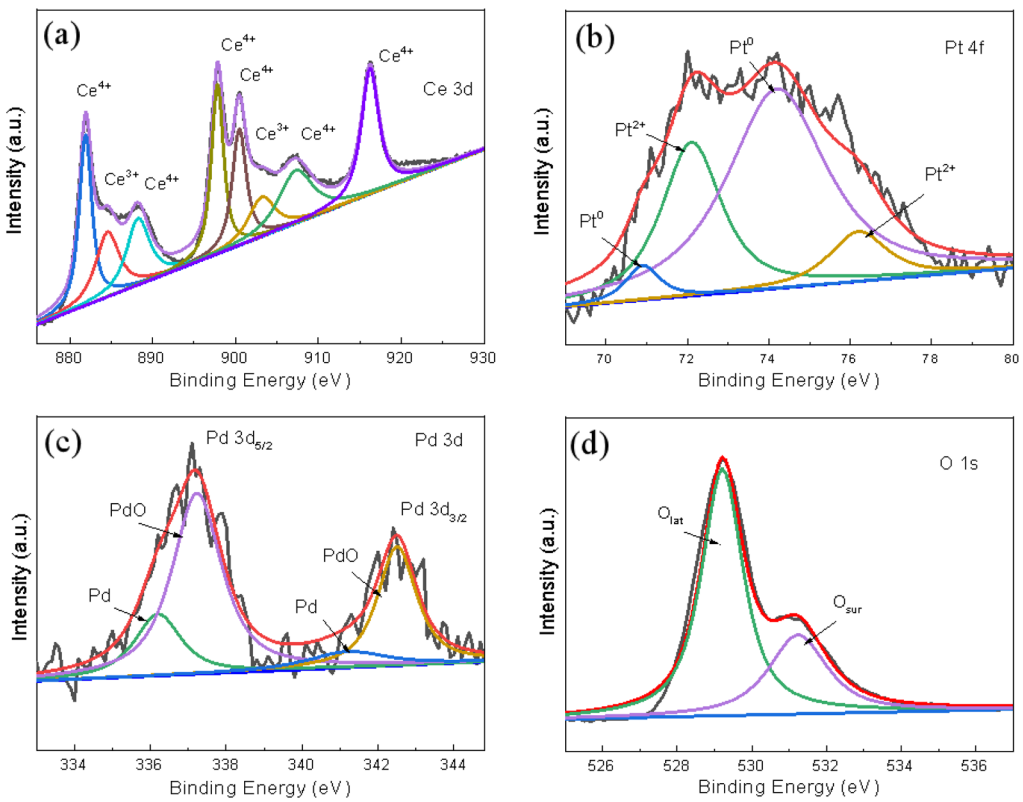

Fig. 6 XPS spectra of (a) Ce 3d, (b) Pt 4f, (c) Pd 3d, (d) O 1s of the $(Pt_{0.1}–Pd_{0.2})/CeO_2$ catalyst.

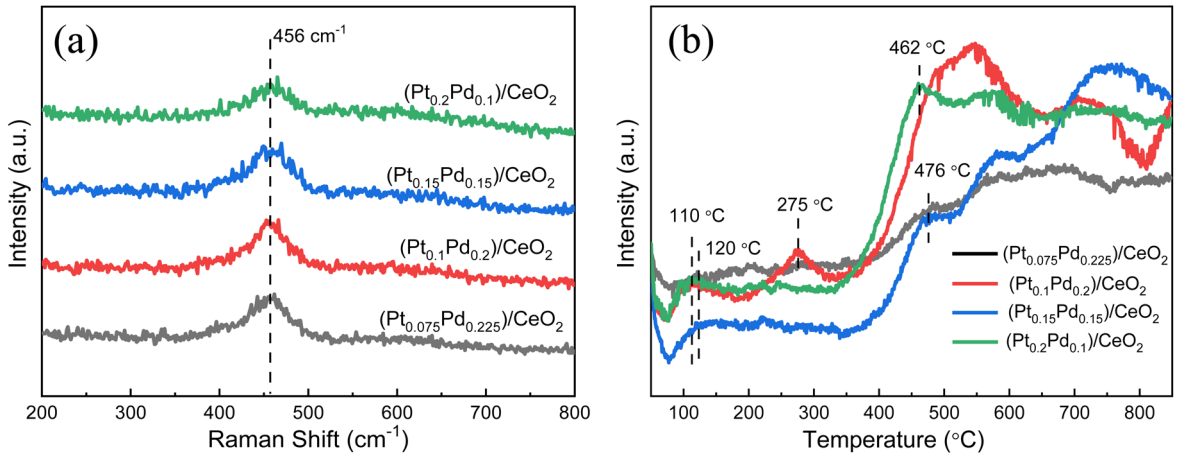

Fig. 7 (a) Raman spectra and (b) H_2-TPR profile of (Pt–Pd)/CeO_2 nanorod supported framework.

$(Pt_{0.15}–Pd_{0.15})/CeO_2$ is significantly higher than that of the other two catalysts, revealing their higher reducibility and superior catalytic performance. Notably, only a reduction peak at 275 °C is observed for the $(Pt_{0.1}–Pd_{0.2})/CeO_2$ catalyst, which may be related to the ionic state of Pt.

The catalytic performance of the (Pt–Pd)/CeO_2 nanorod-supported framework catalysts with varied Pt/Pd content towards CO catalytic oxidation is displayed in Fig. 8. For $Pt_{0.3}/CeO_2$ prepared from de-alloyed $Al_{91.7}Ce_8Pt_{0.3}$ calcined at 573 K, the 50% catalytic CO oxidation temperature (T_{50}) and CO complete conversion temperature (T_{99}) are 91 °C and 113 °C, respectively, which are much better than those for pure CeO_2 calcined at 573 K (T_{50} = 235 °C, T_{99} = 320 °C). The percentage of Pd in the system was continuously increased and when Pt/Pd = 0.2 : 0.1, the catalytic properties were further improved with T_{50} and T_{99} decreasing to 83 °C and 110 °C, respectively. The catalytic performance of the catalyst was the best when Pt/Pd = 0.1 : 0.2, and corresponding 50% and 99% CO conversion temperatures reached as low as 75 °C and 100 °C, respectively. The three repeated catalytic performance tests demonstrate the reproducibility of the $(Pt_{0.2}–Pd_{0.1})/CeO_2$ catalyst (Fig. S5†). By further improving the ratio of Pd to Pt : Pd = 1 : 3, the catalytic performance decreased (T_{50} = 83 °C, T_{99} = 130 °C). Noteworthily, for $(Pt_{0.1}–Pd_{0.2})/CeO_2$ catalyst, the temperature difference between T_{50} and T_{99} is 25 °C, which is smaller than that for catalysts at other Pt/Pd ratios and significantly better than that for pure CeO_2 (80 °C), implying superior catalytic property of (Pt–Pd)/CeO_2 (Fig. 8a). The influence of calcination temperature on the CO conversion rate is also discussed and the data are shown in Fig. 8b. The total CO conversion temperatures of $(Pt_{0.1}–Pd_{0.2})/CeO_2$ at calcination temperatures of 0 °C, 200 °C, 300 °C, 400 °C, 500 °C is 130 °C, 100 °C, 100 °C, 110 °C, 130 °C, respectively, revealed that the catalytic activity is premium at an annealing temperature of 300 °C. The catalytic activity of $(Pt_{0.1}–Pd_{0.2})/CeO_2$ also surpasses that of the state-of-the-art CeO_2-based catalysts reported in the literature, as shown in Table S1.[41–45] †

Fig. 9a explores the influence of O_2 concentration in the feed gas on the catalytic performance of $(Pt_{0.1}–Pd_{0.2})/CeO_2$. The test temperature was maintained at 373 K with a flow rate 100 mL min^{-1}. When 10% O_2 was initially infused into the system, the CO conversion rate could reach 99% because of the sufficient O_2 environment; the CO conversion rate was reduced first

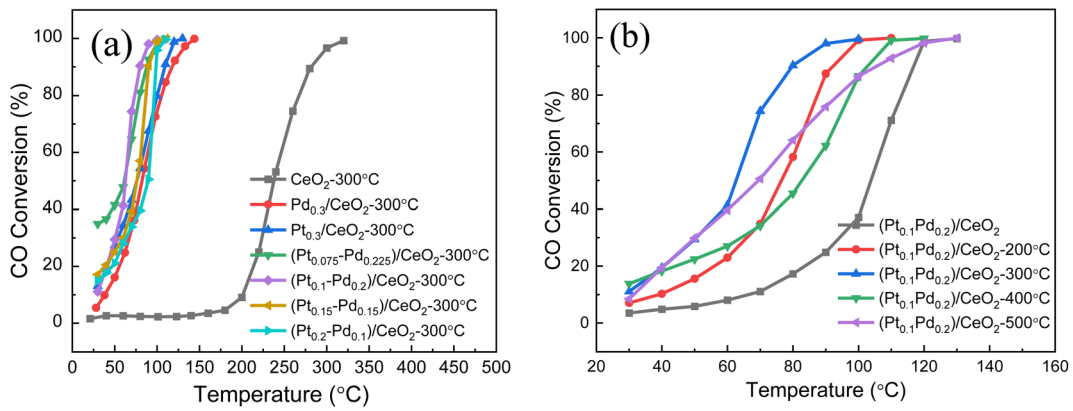

Fig. 8 (a) CO conversion as a function of reaction temperature over the $(Pt_{0.075}–Pd_{0.225})/CeO_2$, $(Pt_{0.1}–Pd_{0.2})/CeO_2$, $(Pt_{0.15}–Pd_{0.15})/CeO_2$ and $(Pt_{0.2}–Pd_{0.1})/CeO_2$ catalysts; (b) the $(Pt_{0.1}–Pd_{0.2})/CeO_2$ catalyst prepared from de-alloyed $Al_{91.7}Ce_8Pt_{0.1}Pd_{0.2}$ calcined at different temperatures.

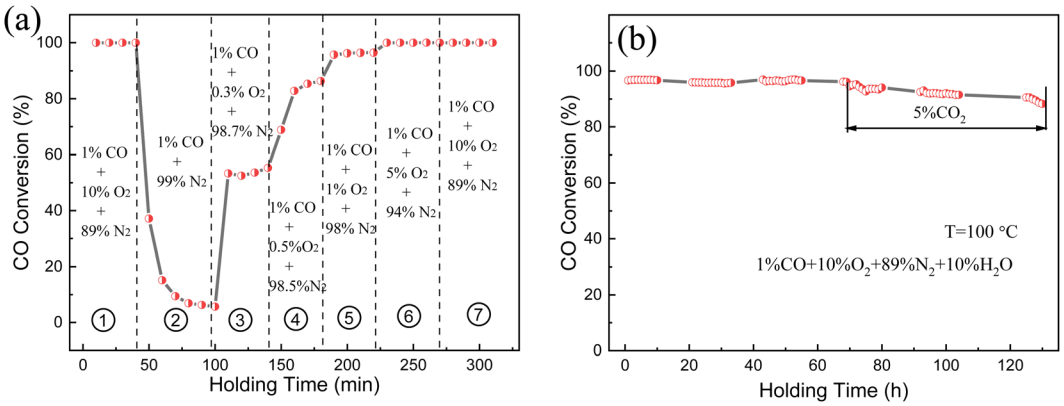

Fig. 9 (a) Catalytic performance under varied oxygen concentrations and (b) long-term stability of the $(Pt_{0.1}–Pd_{0.2})/CeO_2$-573 K catalyst.

and then kept stable at 7% when the O_2 supply was suddenly decreased to zero, which may be ascribed to the existence of surface lattice oxygen that can migrate to active sites and combine with adsorbed CO to form oxygen vacancies. However, the CO conversion rate increases in poor oxygen conditions (0.5–1% O_2) and then recovers to the initial 99% value and remained unchanged when O_2 was resupplied into the feed gas, implying the superior catalytic CO oxidation property of $(Pt_{0.1}–Pd_{0.2})/CeO_2$. The long-term stability and anti-CO_2/H_2O poisoning ability were also investigated and the data are displayed in Fig. 9b. The $(Pt_{0.1}–Pd_{0.2})/CeO_2$ catalyst possesses a 98% conversion rate under the mixed atmosphere of 1% CO, 10% O_2, 89% N_2, 10% H_2O and remained stable without degradation after 70 h of successive reaction; when 5% CO_2 was injected into the infused gas, the adsorption of CO per unit time can be reduced due to the existence of CO competitive adsorption on the surface of $(Pt_{0.1}–Pd_{0.2})/CeO_2$ nanorods, but the CO conversion rate was still maintained around 90% after 60 h, further demonstrating the superior stable catalytic performance and water resistance of the $(Pt_{0.1}–Pd_{0.2})/CeO_2$ catalyst.

A possible mechanism for catalytic CO oxidation on (Pt–Pd)/CeO_2 catalyst is proposed and presented in Scheme 1. Mesoporous structured (Pt–Pd)/CeO_2 catalysts with a high specific surface area can be obtained by introducing Pt and Pd in various proportions. High specific surface area can bring more active sites and provide sufficient reaction paths for catalysis. The (Pt–Pd)/CeO_2 catalyst contains a high concentration of Ce^{3+} ions and active oxygen atoms; the highly concentrated Ce^{3+} can adsorb the required active oxygen on the catalytic interface, which is conducive for the formation of the active centres at the interface. The catalytic performance of the catalyst reached optimum when the same amounts of Pt and Pd were introduced into Al–Ce precursor alloys, which is attributed to the synergetic effect among Pt and PdO nanoparticles, as well as Pt/PdO and CeO_2 nanorods. In the catalytic process, CO is adsorbed onto the surface of Pt and PdO and reacts with oxygen species, which contributes to the formation of CO_2 and oxygen vacancies. The addition of Pt and PdO can accelerate the migration rate of oxygen species, and produce active oxygen species that can combine with activated CO quickly, then the catalytic rate and catalytic performance are enhanced.

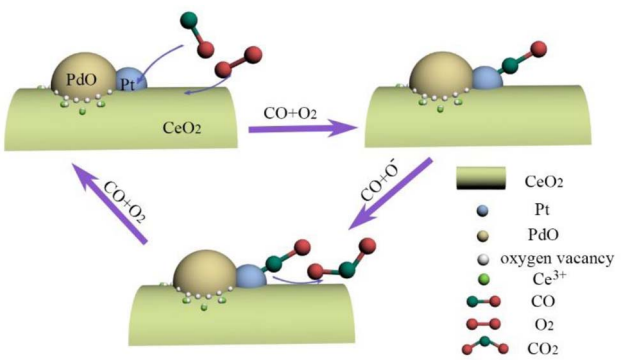

Scheme 1 A possible mechanism for catalytic CO oxidation on (Pt–Pd)/CeO_2 catalyst.

4. Conclusions

In summary, the nanorod-supported nanoporous (Pt–Pd)/CeO_2 catalysts were prepared through a novel dealloying method and calcination treatment. The obtained (Pt–Pd)/CeO_2 prepared from $Al_{91.7}Ce_8Pt_X–Pd_{0.3-X}$ (X = 0, 0.075, 0.1, 0.15, 0.2, 0.3) exhibits an interspersed nanorod structure with rich nanopores distributed among them. The catalytic performance reaches best with a T_{50} temperature of 75 °C and total reaction temperature as low as 100 °C when the Pt/Pd ratio is 0.1 : 0.2. It is believed that the robust framework structure and the synergistic effect of Pt, Pd as well as rich nanopores among nanorods contribute to the high catalytic activity of (Pt–Pd)/CeO_2. These results provide new ideas for the fabrication of catalysts with high catalytic activity by combining earth metal oxides with noble bimetal materials.

Author contributions

Haiyang Wang and Zongcheng Miao conceived the idea and directed the experiments. Wenyuan Duan fabricated all the samples. Ruiyin Zhang, Hao Ma, and Cheng Ma conducted the

characterizations. Miaomiao Liang and Yuzhen Zhao analyzed the data. Haiyang Wang and Wenyuan Duan drafted the manuscript. All the authors discussed the results and reviewed the manuscript.

Conflicts of interest

The authors declare that they have no known competing financial interests or personal relationships that could have appeared to influence the work reported in this work.

Acknowledgements

This work was supported by the National Natural Science Foundation of China (Grant No. 52173263), the Regional Innovation Capability Guidance Program of Shaanxi (No. 2022QFY03-02), the Natural Science Foundation of Anhui Province, China (No. 2108085J11), Natural Science Basic Research Plan in Shaanxi Province of China (Program No. 2022JQ-533), the Scientific Research Program Funded by Shaanxi Provincial Education Department (No. 22JK0595, 22JK0590, 22JK0592, 22JP100), the Fundamental Research Funds for the Central Universities, Northwestern Polytechnical University (No. D5000210825), the Scientific research fund for high-level talents of Xijing University (No. XJ21B17) and the Youth Innovation Team of Shaanxi Universities.

References

1 H. Akimoto, Global air quality and pollution, *Science*, 2003, **302**, 1716–1719.
2 H. Falsig, B. Hvolbaek, I. S. Kristensen, T. Jiang, T. Bligaard, C. H. Christensen and J. K. Norskov, Trends in the catalytic CO oxidation activity of nanoparticles, *Angew. Chem., Int. Ed. Engl.*, 2008, **47**, 4835–4839.
3 H. Zhang, S. Fang and Y. H. Hu, Recent advances in single-atom catalysts for CO oxidation, *Catal. Rev.*, 2020, **64**, 491–532.
4 L. N. Wang, X. N. Li and S. G. He, Recent research progress in the study of catalytic CO oxidation by gas phase atomic clusters, *Sci. China Mater.*, 2019, **63**, 892–902.
5 C. Feng, X. Liu, T. Zhu and M. Tian, Catalytic oxidation of CO on noble metal-based catalysts, *Environ. Sci. Pollut. Res. Int.*, 2021, **28**, 24847–24871.
6 S. W. Chee, J. M. Arce-Ramos, W. Li, A. Genest and U. Mirsaidov, Structural changes in noble metal nanoparticles during CO oxidation and their impact on catalyst activity, *Nat. Commun.*, 2020, **11**, 2133.
7 H. Ha, S. Yoon, K. An and H. Kim, Catalytic CO oxidation over Au nanoparticles supported on CeO_2 nanocrystals: Effect of the Au-CeO interface, *ACS Catal.*, 2018, **8**, 11491–11501.
8 J. Waikar, H. Pawar and P. More, Review on CO oxidation by noble and non-noble metal based catalyst, *Catal. Green Chem. Eng.*, 2019, **2**, 11–24.
9 M. A. van Spronsen, J. W. M. Frenkenb and I. M. N. Groot, Surface science under reaction conditions: CO oxidation on Pt and Pd model catalysts, *Chem. Soc. Rev.*, 2017, **46**, 4347–4374.
10 A. Parinyaswan, S. Pongstabodee and A. Luengnaruemitchai, Catalytic performances of Pt-Pd/CeO_2 catalysts for selective CO oxidation, *Int. J. Hydrogen Energy*, 2006, **31**, 1942–1949.
11 A. De Clercq, O. Margeat, G. Sitja, C. R. Henry and S. Giorgio, Core-shell Pd–Pt nanocubes for the CO oxidation, *J. Catal.*, 2016, **336**, 33–40.
12 C. Garcia, V. Truttmann, I. Lopez, T. Haunold, C. Marini, C. Rameshan, E. Pittenauer, P. Kregsamer, K. Dobrezberger, M. Stoger-Pollach, N. Barrabes and G. Rupprechter, Dynamics of Pd dopant atoms inside Au nanoclusters during catalytic CO oxidation, *J. Phys. Chem. C*, 2020, **124**, 23626–23636.
13 H. J. Kim, M. G. Jang, D. Shin and J. W. Han, Design of Ceria catalysts for low-temperature CO Oxidation, *ChemCatChem*, 2019, **12**, 11–26.
14 F. Maurer, A. Beck, J. Jelic, W. Wang, S. Mangold, M. Stehle, D. Wang, P. Dolcet, A. M. Gänzler, C. Kübel, F. Studt, M. Casapu and J.-D. Grunwaldt, Surface noble metal concentration on Ceria as a key descriptor for efficient catalytic CO oxidation, *ACS Catal.*, 2022, **12**, 2473–2486.
15 K. Polychronopoulou, A. A. AlKhoori, A. M. Efstathiou, M. A. Jaoude, C. M. Damaskinos, M. A. Baker, A. Almutawa, D. H. Anjum, M. A. Vasiliades, A. Belabbes, L. F. Vega, A. F. Zedan and S. J. Hinder, Design aspects of doped CeO_2 for low-temperature catalytic CO oxidation: Transient Kinetics and DFT Approach, *ACS Appl. Mater. Interfaces*, 2021, **13**, 22391–22415.
16 J. Li, Z. Liu, D. A. Cullen, W. Hu, J. Huang, L. Yao, Z. Peng, P. Liao and R. Wang, Distribution and valence state of Ru species on CeO_2 supports: support shape effect and its influence on CO oxidation, *ACS Catal.*, 2019, **9**, 11088–11103.
17 G. Spezzati, A. D. Benavidez, A. T. DeLaRiva, Y. Su, J. P. Hofmann, S. Asahina, E. J. Olivier, J. H. Neethling, J. T. Miller, A. K. Datye and E. J. M. Hensen, CO oxidation by Pd supported on CeO_2(100) and CeO_2(111) facets, *Appl. Catal., B*, 2019, **243**, 36–46.
18 F. Dong, Y. Meng, W. Han, H. Zhao and Z. Tang, Morphology effects on surface chemical properties and lattice defects of Cu/CeO_2 catalysts applied for low-temperature CO oxidation, *Sci. Rep.*, 2019, **9**, 12056.
19 H. Ha, S. Yoon, K. An and H. Kim, Catalytic CO oxidation over Au nanoparticles supported on CeO_2 nanocrystals: Effect of the Au-CeO interface, *ACS Catal.*, 2019, **9**, 12056.
20 A. I. Boronin, E. M. Slavinskaya, A. Figueroba, A. I. Stadnichenko, T. Y. Kardash, O. A. Stonkus, E. A. Fedorova, V. V. Muravev, V. A. Svetlichnyi, A. Bruix and K. M. Neyman, CO oxidation activity of Pt/CeO_2 catalysts below 0 °C: platinum loading effects, *Appl. Catal., B*, 2021, **286**, 119931.
21 H. Jiang, B. Liu, T. Akita, M. Haruta, H. Sakurai and Q. Xu, Au@ZIF-8: CO oxidation over gold nanoparticles deposited to metal-organic framework, *J. Am. Chem. Soc.*, 2009, **131**, 11302–11303.

22 I. McCue, E. Benn, B. Gaskey and J. Erlebacher, Dealloying and de-alloyed materials, *Annu. Rev. Mater. Res.*, 2016, **46**(1), 263–286.
23 Z. Qi and J. Weissmuller, Hierarchical nested-network nanostructure by dealloying, *ACS Nano*, 2013, **7**, 5948–5954.
24 D. Duan, C. Hao, G. He, Y. Wen and Z. Sun, Rh/CeO_2 composites prepared by combining dealloying with calcination as an efficient catalyst for CO oxidation and CH_4 combustion, *J. Rare Earths*, 2022, **40**, 636–644.
25 X. Zhang, D. Duan, G. Li, W. Feng, S. Yang and Z. Sun, Monolithic Au/CeO_2 nanorod framework catalyst prepared by dealloying for low-temperature CO oxidation, *Nanotechnology*, 2018, **29**, 095606.
26 X. Zhang, K. Li, W. Shi, C. Wei, X. Song, S. Yang and Z. Sun, Baize-like CeO_2 and NiO/CeO_2 nanorod catalysts prepared by dealloying for CO oxidation, *Nanotechnology*, 2017, **28**, 045602.
27 T. Kou, C. Si, J. Pinto, C. Ma and Z. Zhang, Dealloying assisted high-yield growth of surfactant-free <110> highly active Cu-doped CeO_2 nanowires for low-temperature CO oxidation, *Nanoscale*, 2017, **9**, 8007–8014.
28 Y. Xiao, H. Li and K. Xie, Activating Lattice Oxygen at the Twisted Surface in a Mesoporous CeO_2 Single Crystal for Efficient and Durable Catalytic CO Oxidation, *Angew. Chem., Int. Ed. Engl.*, 2021, **60**(10), 5240–5244.
29 C. Wang, D. Ren, J. Du, Q. Qin, A. Zhang, L. Chen, H. Cui, J. Chen and Y. Zhao, In Situ Investigations on the Facile Synthesis and Catalytic Performance of CeO_2-Pt/Al_2O_3 Catalyst, *Catalysts*, 2020, **10**(2), 143.
30 X. Zeng, M. Fang, T. Lv, J. Tian, Z. Xia, J. Cen and Q. Wang, Hydrogen-rich gas production by catalytic steam gasification of rice husk using CeO_2-modified Ni-CaO sorption bifunctional catalysts, *Chem. Eng. J.*, 2022, **441**, 136023.
31 Y. Lv, Z. Han, R. Jia, L. Shi and S. Yuan, Porous interface for fast charging silicon anode, *Battery Energy*, 2022, **1**(3).
32 H. Wang, M. Liang, X. Zhang, D. Duan, W. Shi, Y. Song and Z. Sun, Novel CeO_2 nanorod framework prepared by dealloying for supercapacitors applications, *Ionics*, 2018, **24**, 2063–2072.
33 H. Wang, B. Liao, T. Lu, Y. Ai and G. Liu, Enhanced visible-light photocatalytic degradation of tetracycline by a novel hollow BiOCl@CeO_2 heterostructured microspheres: Structural characterization and reaction mechanism, *J. Hazard. Mater.*, 2020, **385**, 121552.
34 L. Yu, T. Zhou, S. Cao, X. Tai, L. Liu and Y. Wang, Suppressing the surface passivation of Pt-Mo nanowires *via* constructing Mo-Se coordination for boosting HER performance, *Nano Res.*, 2020, **14**, 2659–2665.
35 J. Li, H. Huang, Y. Li, Y. Tang, D. Mei and C. Zhong, Stable and size-controllable ultrafine Pt nanoparticles derived from a MOF-based single metal ion trap for efficient electrocatalytic hydrogen evolution, *J. Mater. Chem. A*, 2019, **7**, 20239–20246.
36 X. Li, J. Feng, M. Perdjon, R. Oh, W. Zhao, X. Huang and S. Liu, Investigations of supported Au-Pd nanoparticles on synthesized CeO_2 with different morphologies and application in solvent-free benzyl alcohol oxidation, *Appl. Surf. Sci.*, 2020, **505**, 144473.
37 K. Chen, X. Zhao, X.-J. Zhang, W.-S. Zhang, Z.-F. Wu, H.-Y. Wang, D.-X. Han and L. Niu, Enhanced photocatalytic CO_2 reduction by constructing an In_2O_3-CuO heterojunction with CuO as a cocatalyst, *Catal. Sci. Technol.*, 2021, **11**, 2713–2717.
38 S. T. Hossain, Y. Almesned, K. Zhang, E. T. Zell, D. T. Bernard, S. Balaz and R. Wang, Support structure effect on CO oxidation: A comparative study on SiO_2 nanospheres and CeO_2 nanorods supported CuO_x catalysts, *Appl. Surf. Sci.*, 2018, **428**, 598–608.
39 B. Han, H. Li, L. Li, Y. Wang, Y. Zhang and G. Li, Kinetic control of CeO_2 nanoparticles for catalytic CO oxidation, *J. Mater. Res.*, 2019, **34**, 2201–2208.
40 J. Wang, J. Zhong, M. Gong, Z. Liu, M. Zhao and Y. Chen, Remove cooking fume using catalytic combustion over Pt/La-Al_2O_3, *J. Environ. Sci.*, 2007, **19**, 644–646.
41 Y. Deng, P. Tian, S. Liu, H. He, Y. Wang, L. Ouyang and S. Yuan, Enhanced catalytic performance of atomically dispersed Pd on Pr-doped CeO_2 nanorod in CO oxidation, *J. Hazard. Mater.*, 2022, **426**, 127793.
42 C. Zong, C. Wang, L. Hu, R. Zhang, P. Jiang, J. Chen, L. Wei and Q. Chen, The Enhancement of the Catalytic Oxidation of CO on Ir/CeO(2) Nanojunctions, *Inorg. Chem.*, 2019, **58**, 14238–14243.
43 H. Li, M. Shen, J. Wang, H. Wang and J. Wang, Effect of Support on CO Oxidation Performance over the Pd/CeO_2 and Pd/CeO_2-ZrO_2 Catalyst, *Ind. Eng. Chem. Res.*, 2020, **59**, 1477–1486.
44 J. Zhen, X. Wang, D. Liu, Z. Wang, J. Li, F. Wang, Y. Wang and H. Zhang, Mass production of Co_3O_4@CeO_2 core@shell nanowires for catalytic CO oxidation, *Nano Res.*, 2015, **8**, 1944–1955.
45 Y. Wang, C. Pei, Z. Zhao and J. Gong, Kinetically rate-determining step modulation by metal-support interactions for CO oxidation on Pt/CeO_2, *Sci. China: Chem.*, 2022, **65**, 2038–2044.